

Wedge Waveguides and Resonators for Quantum Plasmonics

Stephan J. P. Kress,[†] Felipe V. Antolinez,[†] Patrizia Richner,[‡] Sriharsha V. Jayanti,^{†,§} David K. Kim,[†] Ferry Prins,[†] Andreas Riedinger,[†] Maximilian P. C. Fischer,[†] Stefan Meyer,[†] Kevin M. McPeak,[†] Dimos Poulikakos,[‡] and David J. Norris^{*,†}

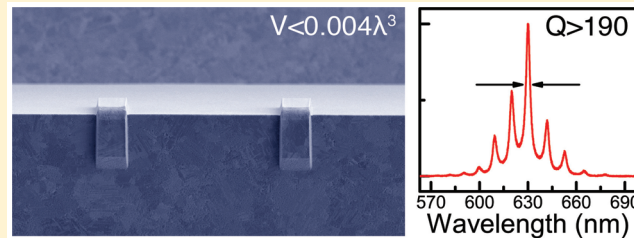
[†]Optical Materials Engineering Laboratory, ETH Zurich, 8092 Zurich, Switzerland

[‡]Laboratory of Thermodynamics in Emerging Technologies, ETH Zurich, 8092 Zurich, Switzerland

[§]Department of Chemical Engineering and Materials Science, University of Minnesota, Minneapolis, Minnesota 55455, United States

Supporting Information

ABSTRACT: Plasmonic structures can provide deep-subwavelength electromagnetic fields that are useful for enhancing light–matter interactions. However, because these localized modes are also dissipative, structures that offer the best compromise between field confinement and loss have been sought. Metallic wedge waveguides were initially identified as an ideal candidate but have been largely abandoned because to date their experimental performance has been limited. We combine state-of-the-art metallic wedges with integrated reflectors and precisely placed colloidal quantum dots (down to the single-emitter level) and demonstrate quantum-plasmonic waveguides and resonators with performance approaching theoretical limits. By exploiting a nearly 10-fold improvement in wedge-plasmon propagation ($19\ \mu\text{m}$ at a vacuum wavelength, λ_{vac} , of $630\ \text{nm}$), efficient reflectors (93%), and effective coupling (estimated to be >70%) to highly emissive (~90%) quantum dots, we obtain Ag plasmonic resonators at visible wavelengths with quality factors approaching 200 (3.3 nm line widths). As our structures offer modal volumes down to $\sim 0.004\lambda_{\text{vac}}^3$ in an exposed single-mode waveguide–resonator geometry, they provide advantages over both traditional photonic microcavities and localized-plasmonic resonators for enhancing light–matter interactions. Our results confirm the promise of wedges for creating plasmonic devices and for studying coherent quantum-plasmonic effects such as long-distance plasmon-mediated entanglement and strong plasmon–matter coupling.



KEYWORDS: Plasmonic waveguides, plasmonic resonators, quantum plasmonics, semiconductor nanocrystals, colloidal quantum dots, nanophotonics

One goal of quantum optics is to influence light–matter interactions.¹ When quantum emitters are placed in a confined electromagnetic field, their optical properties (e.g., emission rate² or direction³) can be controlled, and coherent phenomena such as superradiance, quantum entanglement, and strong emitter–field coupling can be induced.⁴ However, these effects, which are inversely proportional to the volume of the field, are limited by diffraction in traditional quantum optics. Nanophotonics provides a potential route to increase the interactions further by exploiting more tightly confined modes.⁵ For example, surface-plasmon polaritons (SPPs), which are hybrid electron–photon waves at metal–dielectric interfaces,⁶ can concentrate light to the nanoscale.^{7,8} This can be useful not only for creating nanoscale optical devices and circuits^{9,10} but also for exploring enhanced light–matter interactions via quantum plasmonics.^{11–13}

Unfortunately, plasmonic structures also exhibit losses, which increase with increasing field confinement. In general, these losses arise from both intrinsic dissipation in the material and imperfections in the fabricated structure. If the latter could be completely eliminated, an important question would be which designs offer the best compromise between modal volume and

intrinsic loss.¹⁴ Significant effort has focused on identifying such designs for quantum plasmonics.^{15,16}

From a theoretical perspective, a versatile strategy (exploited in conventional quantum optics) is to combine a single-mode waveguide with two reflectors to form a resonator.¹³ This approach can utilize the many structures that have been investigated for plasmonic waveguides, including stripes,¹⁷ nanowires,^{18,19} channels,^{20–24} wedges,^{25–28} and hybrids.^{10,14,29} Among these, calculations have shown that wedge waveguides can offer the smallest modal size for a given propagation length.^{14,26} However, because of fabrication difficulties, wedge waveguides have not yet fulfilled this promise. If high-quality wedges were available, end reflectors could be added to create a resonator. Previous work has shown that the intrinsic reflectivity at the bare end of a plasmonic waveguide (e.g., a nanowire) is only 20–30%.^{18,30} While distributed Bragg reflectors have been employed to increase this,³¹ geometrically simple “block” reflectors offer better performance.^{32,33} Thus,

Received: August 2, 2015

Published: August 18, 2015

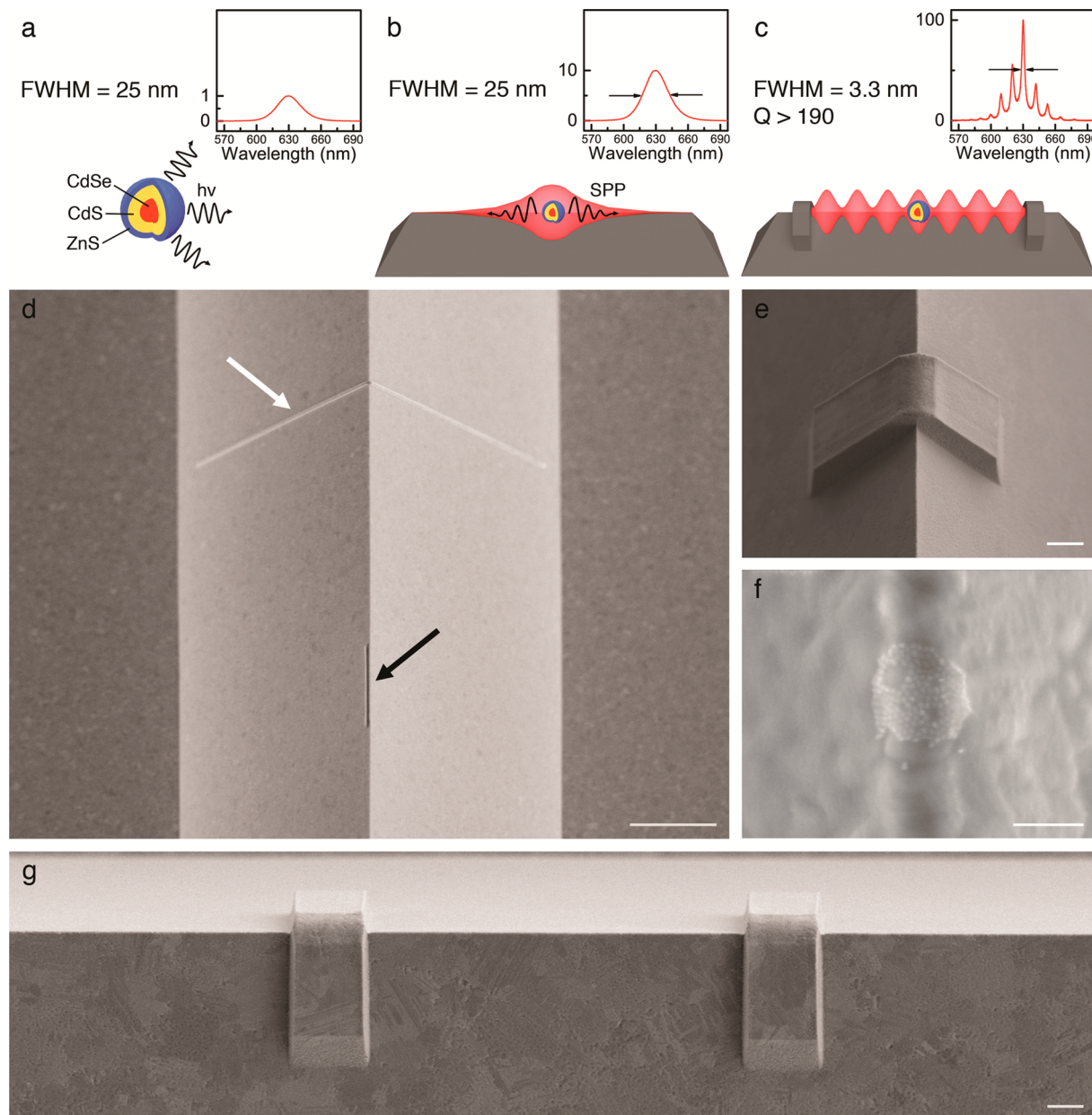


Figure 1. Quantum dot (QD) plasmonic components. (a–c) Schematics of CdSe/CdS/ZnS core/shell/shell QDs (a) in free space, (b) on a wedge waveguide, and (c) on a wedge resonator. In each case, the expected QD emission spectrum is depicted (not to scale). The QD line width should narrow when on the resonator because of the plasmonic Fabry-Pérot modes. In (b) and (c) the excited wedge-plasmon polaritons (WPPs) are depicted in red. (d) Scanning electron micrograph of a Au wedge waveguide with an integrated bump line (white arrow) and QDs (black arrow) printed along the apex (scale bar = 5 μ m). (e) Ag wedge waveguide with an integrated block reflector with a height of 600 nm (scale bar = 1 μ m). (f) QDs printed onto the apex of a Ag wedge (scale bar = 100 nm). (g) Side view of a Ag wedge resonator with block heights of 600 nm and \sim 100 QDs (not visible at this magnification) printed along the apex (scale bar = 1 μ m).

wedge waveguides with such reflectors provide a potentially ideal yet unexplored plasmonic resonator.

To exploit these to study light–matter interactions via waveguide quantum electrodynamics (wQED), quantum emitters must be integrated at specific locations. Candidates include molecular dyes,³⁴ nitrogen vacancies (NVs),^{30,31} and colloidal semiconductor quantum dots.^{3,31,35,36} Early work on plasmonic wQED combined NVs with randomly placed colloidal Ag nanowires.³⁰ To control the interactions, it would be preferable to place the emitters precisely in the resonator.²⁴

Here we address all of these challenges and demonstrate state-of-the-art plasmonic wedge waveguides and resonators with integrated colloidal quantum dots (QDs).^{37,38} We focus primarily on Ag wedges, as they provide the best (and possibly ultimate³⁹) plasmonic performance at visible wavelengths, but results are also shown for Au. We optimized each aspect of the structure, starting with the metal itself. We deposited Ag films with optical properties comparable to those of single crystals.⁴⁰ We then fed the measured dielectric functions into simulations to determine the ideal wedge geometry. After fabricating the required waveguides and block reflectors with near-atomically flat surfaces using template stripping,^{41,42} we placed either

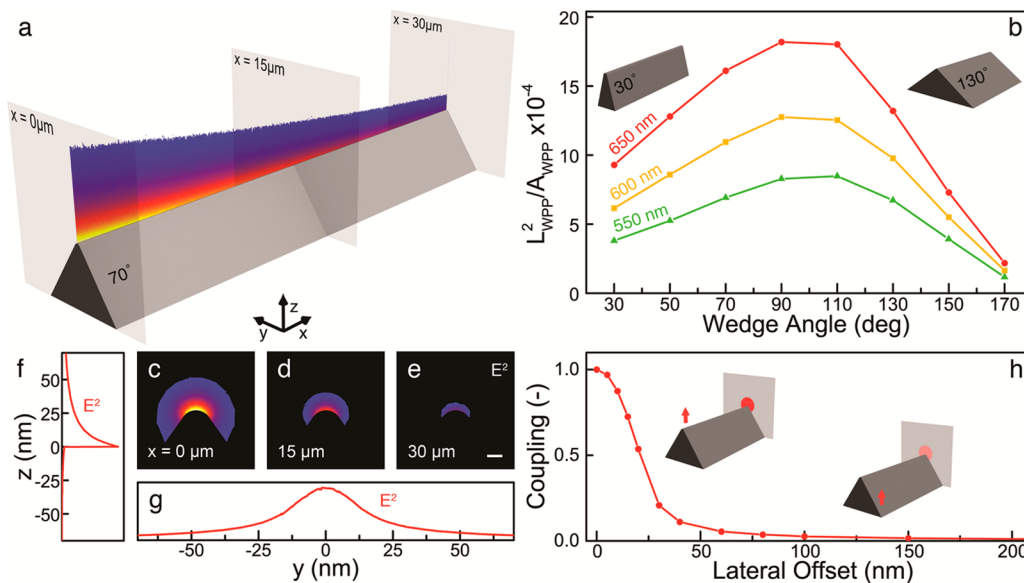


Figure 2. Optimization of wedge waveguides for quantum plasmonics. (a) 3D electromagnetic simulation of a wedge-plasmon polariton (WPP) propagating along the apex of a Ag wedge. (b) Calculated performance of Ag wedge waveguides in terms of the squared propagation length, L_{WPP}^2 , divided by the effective modal area, A_{WPP} , plotted versus the wedge angle for vacuum wavelengths of 550, 600, and 650 nm (also see Section 3 and Figure S4 in the Supporting Information). The measured dielectric functions for Ag (Figure S1) and a 20 nm radius of curvature at the apex (Figure S3) are assumed. (c–e) Relative cross sections of the field intensity of the WPP from (a) at $x = 0, 15$, and $30 \mu\text{m}$ (scale bar = 10 nm). (f, g) Electric-field intensities plotted in the vertical (z) and horizontal (y) directions. (h) Simulated coupling between a vertically aligned dipole and the WPP mode as a function of the lateral offset of the dipole along the wedge face. The dipole was placed 10 nm above the surface. (Also see Section 3 and Figure S6 in the Supporting Information).

multiple or individual QDs with nanometer precision on the wedge using a special type of electrohydrodynamic (EHD) printing.^{43,44} The final structures exhibit behavior confirming the promise of wedge waveguides. We observe efficient emitter–waveguide coupling, single subdiffraction plasmonic modes with long propagation, and plasmonic resonators with high quality factors, Q , all in agreement with theoretical simulations.

Colloidal semiconductor QDs are ideal emitters for light–matter interactions because of their efficient emission and large dipole moments. For example, we exploit state-of-the-art colloidal CdSe/CdS/ZnS core/shell/shell QDs^{37,38} (Figure 1a) that exhibit bright (quantum yields of ~90% in liquid dispersions) and narrow (full width at half-maximum, fwhm, of 25 nm) emission lines centered at 630 nm, which are well-suited to Ag plasmonics. If these emitters are placed in the near field of a plasmonic wedge waveguide, we expect photo-excitation of the QDs to lead to an intense SPP beam along the apex of the metallic wedge (Figure 1b). Emission into this waveguide mode should be enhanced by the Purcell effect⁴⁵ (along with increased coupling) due to the higher density of electromagnetic modes near the wedge. A further increase should occur if the wedge plasmons are constrained in a resonator by block reflectors. Interference between the counterpropagating plasmons should lead to Fabry–Pérot modes in the resonator (Figure 1c).

To realize such resonators, we first formed triangular trenches in (100)-oriented silicon wafers via anisotropic etching.⁴⁶ The sides of such trenches, which are defined by the Si(111) atomic planes, are extremely smooth with a precise relative angle of 70.54° . By evaporating >350 nm of Ag or Au onto this trench and peeling this film off via template stripping,⁴¹ ultrasMOOTH wedges with sharp apexes are revealed⁴² (Figure 1d). We also modified this process to

incorporate several additional components. First, we included “bump lines” across the waveguides (white arrow in Figure 1d) to act as outcouplers for probing plasmon propagation. These were obtained by milling a shallow groove (typically 200 nm wide by 60 nm deep) across the Si trench with a focused ion beam (FIB) prior to metal deposition. Second, we added block reflectors (Figure 1e) by milling deeper grooves (0.6–1.2 μm deep, 2 μm wide, and 5 μm across) into the Si trench. Third, after the wedges were prepared, we placed our QDs precisely on the apex of the waveguides (black arrow in Figure 1d) by exploiting EHD NanoDrip printing.^{43,44} This technique allows precise placement of countable numbers of QDs (Figure 1f), down to individual emitters. Figure 1g shows a complete Ag wedge resonator ($10 \mu\text{m}$ cavity length) with ~100 QDs placed on the apex (not visible at this magnification).

Among the many possible plasmonic waveguides, wedges offer extremely small mode sizes while still maintaining relatively long plasmon-propagation lengths.¹⁴ This allows quantum emitters to couple efficiently to the confined mode and transmit signals over long distances, both of which are essential features for applications and wQED.^{13,47} However, the performance of the waveguide is also affected by the specific geometry of the wedge. To determine the optimal structure, we used finite-element simulations (COMSOL Multiphysics) to analyze the propagation of the wedge-plasmon polaritons (WPPs) along wedges of a given geometry (Figure 2a). Using experimentally measured dielectric functions for our Ag (see Figure S1 in the Supporting Information), we performed modal analyses for WPPs at vacuum wavelengths of 550, 600, and 650 nm propagating on wedges of various angles (see Section 3 and Figure S2 in the Supporting Information). The apex was rounded with a 20 nm radius, consistent with cross-sectional measurements of our experimental structures ($20 \pm 1 \text{ nm}$; see Figure S3). Figure 2b plots the results in terms of a

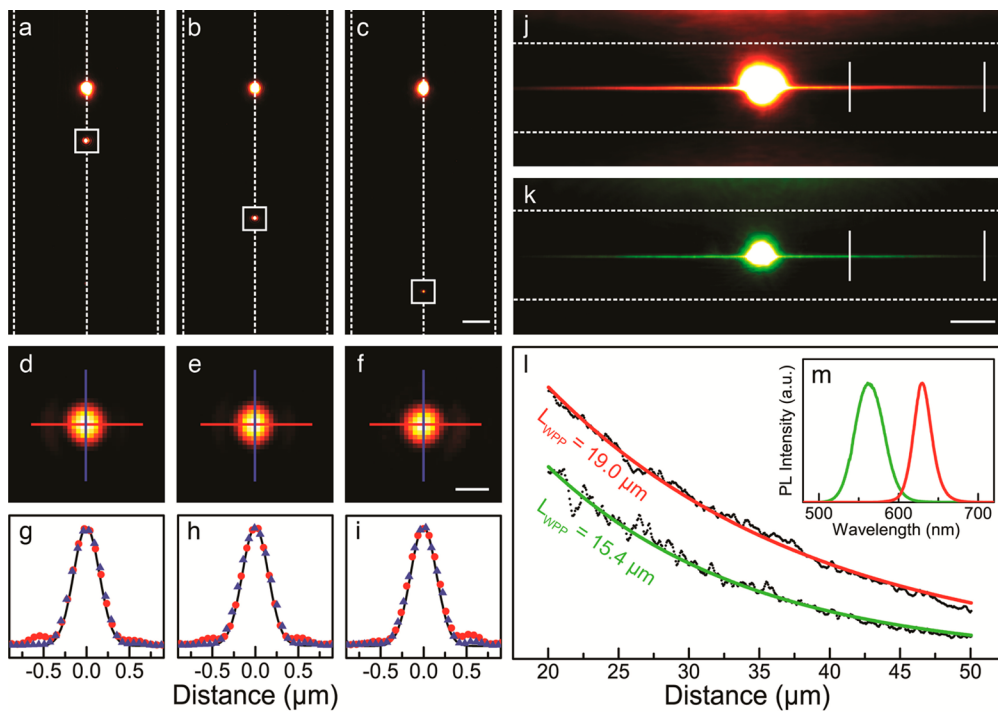


Figure 3. Characterization of single-mode, deep-subdiffraction wedge-plasmon polaritons (WPPs). (a–c) False-color fluorescence micrographs of QDs (bright spots, emission peak at 630 nm) placed on the apexes (dashed vertical lines in the image centers) of Ag wedges at different distances from bump lines. WPPs are launched by the QDs and scatter light (squares) at the bumps (scale bar = 5 μm). (d–f) Magnified views of the scattered light from the bump lines in (a–c), normalized for comparison (scale bar = 500 nm). (g–i) Spatial cross sections of the scattered signals in (d–f) in the x direction (blue) and the y direction (red) compared with the expected signal of an ideal point dipole (black line). (j, k) False-color fluorescence micrographs from Ag wedges with QDs emitting at 630 and 564 nm, respectively. The bright spots in the center are direct fluorescence. With long exposure times, weak scattered light from WPPs propagating along the wedge apexes is detected as horizontal streaks on either side (scale bar = 10 μm). The horizontal dashed lines show the bases of the wedges. (l) Intensity profiles plotted along the wedge between the vertical lines in (j, k), yielding propagation lengths of 19.0 and 15.4 μm for WPPs generated by red and green QDs, respectively. (m) Fluorescence spectra of the red and green QDs.

dimensionless figure of merit¹³ (FOM), the squared propagation length, L_{WPP}^2 , divided by the effective modal area, A_{WPP} . (Figure S4 plots these parameters separately.) We found that the FOM is maximized for relatively blunt angles ranging from 90 to 110°. This indicates that previous results^{25,26,28,48} obtained for very sharp wedges (20–40°) were suboptimal for wQED.

Fortunately, anisotropic etching automatically provides 70° wedges, which exhibit nearly 90% of the maximum performance. Our simulations show that such waveguides should support single-mode subdiffraction WPPs that exponentially decay along the apex (Figure 2a), in agreement with earlier studies.^{25,26,28,48} Figure S5 plots the dispersion for these WPPs. Simulated modal cross sections at 0, 15, and 30 μm are shown in Figure 2c–e, along with the profiles in the z direction (Figure 2f) and the y direction (Figure 2g). The local field intensity, which depends on the apex radius,²⁸ has a maximum that decays rapidly within 10–20 nm of the tip.

This is ideal for coupling to our core/shell/shell QDs, which are 14 nm in total diameter but have a dipolar exciton primarily confined to the inner 4.1 nm core. For flat metals, excited dipoles should be separated by ~10 nm to optimize emitted plasmons while avoiding excessive quenching.^{13,49} Because the fields are more confined in the wedge, the best separation is likely less than 10 nm. This could be achieved with a uniform dielectric layer, but this would decrease the propagation of the WPPs. Instead, we exploit the shells of our QDs, which not only enhance the fluorescence efficiency^{37,38} but automatically

place the core ~5 nm away from the metal. The shell also provides a separation layer only at the emitter, maintaining good performance elsewhere.

Another important consideration is the lateral placement of the QDs. We calculated the relative emitter–waveguide coupling for a vertically aligned dipolar emitter that is offset from its ideal alignment with the waveguide (Figure 2h). The coupling decreases by more than 50% when the dipole is displaced laterally only 20 nm down the wedge face. Similar results were obtained for a dipole oriented normal to the wedge (Figure S6). This confirms the need for precise placement of the QDs.

Figure 3 characterizes the plasmonic properties of our Ag wedges. QDs with an emission maximum at 630 nm were printed onto waveguides that included bump lines at three distances (Figure 3a–c). Upon photoexcitation of the QDs (bright spots in Figure 3a–c), WPPs are launched along the wedge and scatter into photons at the bump lines (squares in Figure 3a–c). These scattering signals decay with increasing distance from the QDs, indicative of propagating WPPs. When the intensities of these signals are normalized (Figure 3d–f), their spatial extents are identical within measurement error. This is confirmed by the cross sections (Figure 3g–i) in the x direction (blue) and the y direction (red). Further, these scattering signals are within 10% of that for an ideal point dipole emitting at 630 nm (approximated by a Gaussian). Similar results are shown for Au wedges in Figure S7. Because the bump lines are extended along the wedge faces, the lack of

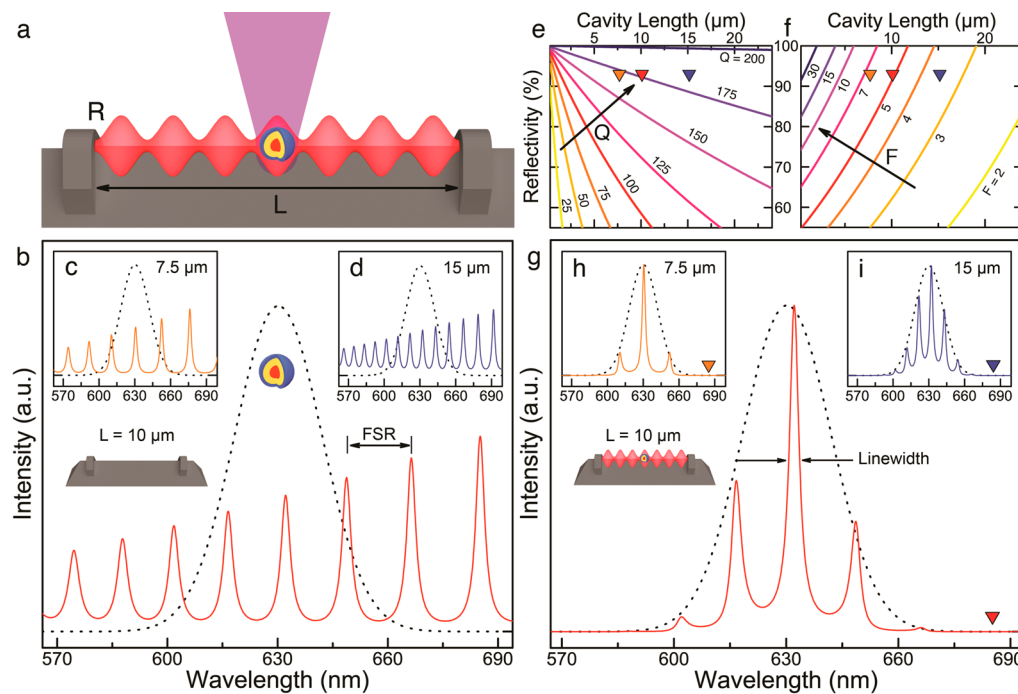


Figure 4. Simulation of quantum-plasmonic resonators. (a) Schematic of a quantum-plasmonic resonator of length L with blocks of reflectivity R . When quantum dots (QDs) are photoexcited (violet), wedge-plasmon polaritons (WPPs) with propagation length L_{WPP} induce Fabry–Pérot modes (red). (b–d) Simulated resonator spectra for cavities of length 10, 7.5, and 15 μm and blocks of 93% reflectivity. The expected emission spectrum for our red QDs, approximated by a Gaussian (dashed line), is shown for comparison. Similar to photonic Fabry–Pérot resonators, the mode spacing, or free spectral range (FSR), is inversely proportional to L . In all resonators, dispersion causes the resonances to narrow at longer wavelengths. (e, f) Contour plots of the predicted resonator quality factor, Q , and finesse, F , as a function of R and L at a free-space wavelength of 630 nm. (g–i) Predicted QD–resonator spectra for cavities of length 10, 7.5, and 15 μm and blocks of 93% reflectivity. The positions of these resonators on the contour plots in (e, f) are indicated by orange (7.5), red (10), and blue (15 μm) triangles.

scattering on the faces confirms that near-field dipolar sources (such as QDs) can excite subdiffraction WPPs that propagate only along the apex, as expected from Figure 2.

By increasing both the intensity of the excitation light and the exposure time of our camera, we could detect weak scattering from the WPPs during propagation. These are seen as horizontal streaks in Figure 3j,k for red- and green-emitting QDs, respectively. They represent WPPs decaying as they propagate away from the printed QDs along the wedge apexes. We extracted the intensities of these streaks between 20 and 50 μm from the QD source (Figure 3l). The propagation lengths were 19.0 and 15.4 μm for QDs emitting at 630 and 564 nm (Figure 3m), respectively. The value at 630 nm is nearly an order of magnitude longer than previously reported for wedge waveguides.^{25,28} We note that this improvement depended greatly on the metal-deposition conditions. Even when we used template stripping but deposited our Ag under nonoptimal (albeit common) conditions, dramatically worse propagation of WPPs was observed (Figure S8).

On the basis of the deliberate overexposure in the images in Figure 3j,k, one may incorrectly conclude that the QDs emit mostly photons and are poorly coupled to the waveguide. In fact, for all of the wedges investigated, the QDs generated more WPPs than photons (see Figure S9). QDs that were well-placed on the waveguide emitted >2.5 times more WPPs (even higher values were observed for the resonators discussed below). From such measurements, we estimated the fraction of energy emitted into the waveguide mode, also known as the beta factor. Neglecting nonradiative losses, the experimental beta factor was estimated to be >70%, which is comparable to

predictions of 90%.⁴⁸ Since our values are averaged over an ensemble of QDs, individual QDs should experience even higher coupling.

Plasmonic resonators should then result from these structures if efficient reflectors are introduced. QDs sitting on the apex of the wedge should couple strongly to this resonator and excite its plasmonic modes (Figure 4a). To predict the expected cavity spectra, we first calculated the Fabry–Pérot resonances of the wedge. These depend on the cavity length, L , the propagation length of the WPPs, L_{WPP} , and the reflectivity of the reflectors, R . Figure 4b–d shows the predicted spectra for three cavity lengths. The emission spectrum of our red-emitting QDs, approximated as a Gaussian (dashed line), is included for comparison. We used the measured value for L_{WPP} (19 μm ; Figure 3l) and 93% for R , consistent with predictions for typical block-reflector heights³³ (see Section 3 and Figure S10 in the Supporting Information). As in photonic Fabry–Pérot cavities, the plasmonic resonator exhibits a doubling of the free spectral range (FSR) when L is halved from 15 to 7.5 μm . However, in contrast to photonic cavities, the plasmonic resonances narrow and grow in intensity at longer wavelengths as a result of strong dispersion in the metal.

Because each round trip in the plasmonic resonator involves losses due to both propagation and the reflectors, the cavity quality factor, Q , which describes the spectral line width, and the cavity finesse, F , which characterizes the modulation depth, have opposite trends. Figure 4e,f presents contour plots of these parameters at 630 nm as functions of R and L . For a given reflectivity, Q decreases with cavity size. Smaller cavities lead to more reflections and thus more loss per unit time, reducing the

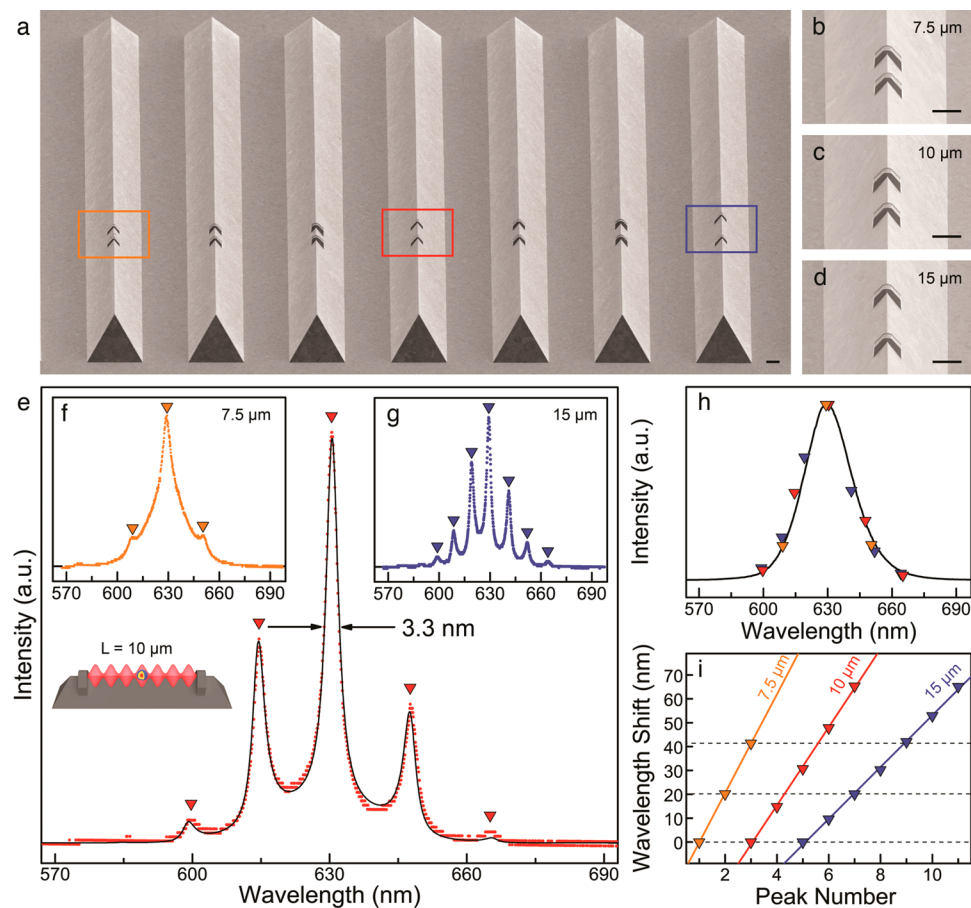


Figure 5. Measurements of quantum-plasmonic resonators. (a) Scanning electron micrograph of an array of 300 μm long Ag wedges with 7.5 μm (wedges 1 to 3 from the left), 10 μm (wedges 4 to 6), and 15 μm (wedge 7) resonators (scale bar = 5 μm). The heights of the block reflectors are 600 nm (wedges 1, 4, and 7), 900 nm (wedges 2 and 5), and 1200 nm (wedges 3 and 6). (b–d) Magnified images of three resonators with 900 nm high block reflectors (scale bars = 5 μm). The quantum dots (QDs) are not visible since only \sim 100 QDs were placed in each cavity to avoid unnecessary damping. (e–g) Measured spectra for the 7.5, 10, and 15 μm resonators highlighted with boxes in (a). Each has 600 nm high block reflectors. The WPP signal is collected as light scattered from one of the reflectors. In (e), a fit using the dispersive quantum-plasmonic model (Figure 4) is also presented (black line). (h) Peak positions of the three cavities from (e–g) (red, orange, and blue triangles) overlaid with the emission spectrum from QDs not in the cavity (black line). (i) Peak positions and a linear fit for each resonator relative to its shortest-wavelength peak. The resonances are approximately equally spaced, and doubling the cavity length halves the FSR, as expected.

lifetime of the WPP in the resonator. In contrast, F is inversely related to the cavity size. Larger cavities have larger round-trip loss, leading to less interference and reduced finesse.

If a quantum emitter is coupled to our wedge resonator, its emission should be enhanced as a result of the Purcell effect when it is resonant with a cavity mode.⁴⁵ Thus, the approximately Gaussian QD-emission spectrum, E_{QD} , should be multiplied by the resonator spectrum, I_{res} , to yield

$$I_{\text{QD-res}}(\nu) = I_{\text{res}}(\nu)E_{\text{QD}}(\nu)$$

$$= \frac{I_0}{[1 - r(\nu)]^2 + 4r(\nu) \sin\left(\frac{\pi\nu}{\nu_{\text{FSR}}(\nu)}\right)}$$

$$\exp\left[-\frac{(\nu - \nu_{\text{peak}})^2}{2\sigma^2}\right]$$

where I_0 is the intensity of the initial wave in the cavity,⁵⁰ ν is the frequency, ν_{FSR} is the FSR, ν_{peak} is the frequency of the QD-emission peak, σ is the QD line width (standard deviation), and r is the round-trip loss (see Section 7 in the Supporting Information). Figure 4g–i shows plots of the predicted QD–

resonator spectra for three cavity sizes. Clearly, the resonator should dramatically alter the QD-emission spectrum as WPPs are launched at the resonance frequencies. Further, as shown by the triangles in Figure 4e,f, which place these spectra on the contour plots for Q and F , reasonable values can be expected.

To test this, we fabricated a series of Ag wedge resonators on the same substrate (Figure 5a). Magnified views of 7.5, 10, and 15 μm cavities are shown in Figure 5b–d. Each resonator contains \sim 100 QDs (not visible). This number was chosen to allow excitation of the plasmonic modes without introducing any unnecessary damping. Upon illumination of the QDs with blue light, the QDs interact with the plasmonic modes in the cavity. This was confirmed by collecting scattered photons from one of the block reflectors with a microphotoluminescence setup. The experimental spectra are shown in Figure 5e–g, which clearly resemble the predictions in Figure 4. The 10 μm resonator exhibits a line width of 3.3 nm at the central peak, which indicates a Q of 191. At visible wavelengths, such high quality factors have so far only been attained for planar, nonwaveguiding plasmonic cavities³³ that are less suited to quantum plasmonics because of their multimode nature and higher modal volumes.

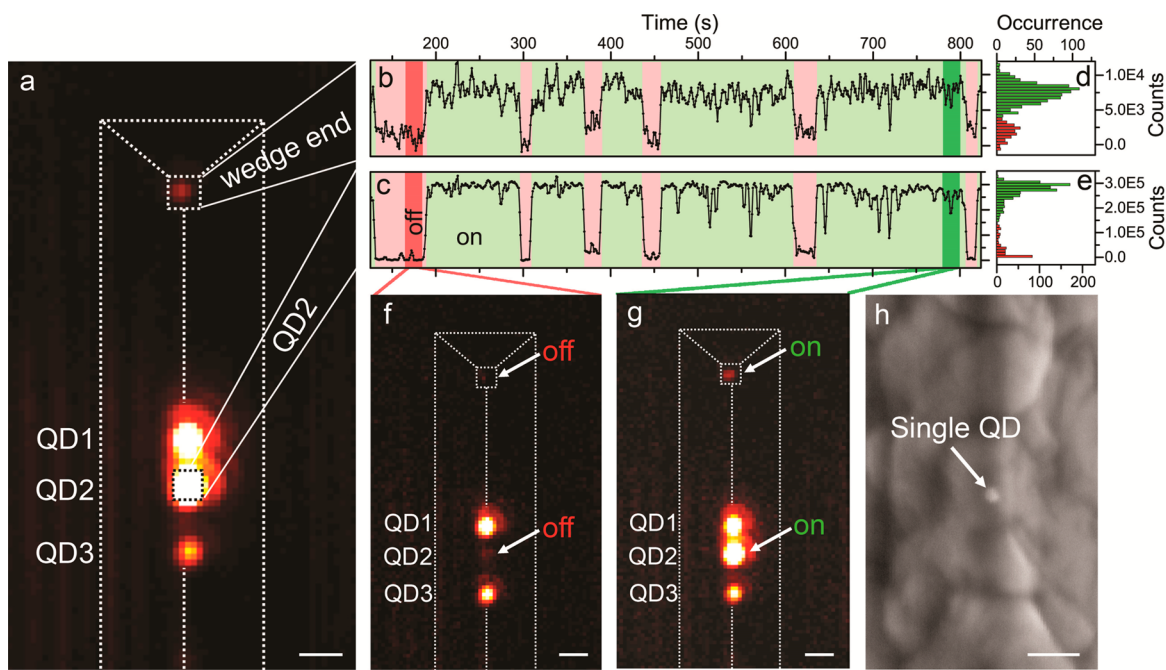


Figure 6. Single-quantum-dot quantum plasmonics. (a) False-color fluorescence micrograph (integrated from a time series of 1000 images with 1 s exposure time) of three individual quantum dots (QD1, QD2, and QD3) on the apex of a Ag wedge (scale bar = 1 μm). Plasmons generated by the three QDs scatter at the top end of the wedge. See also Movie S1 in the Supporting Information. (b, c) Time series for the fluorescence intensities extracted from (b) the wedge end and (c) QD2. The two signals are strongly correlated and exhibit on and off periods (highlighted in green and red, respectively) characteristic of single-QD emission. (d, e) The bimodal distribution in intensities is also seen in histograms for (d) the wedge end and (e) QD2. In (f) and (g), intensities were integrated over 20 frames of the off state (frames 166–185) and on state (frames 780–799) (scale bars = 1 μm). (h) High-resolution scanning electron micrograph of an individual QD on the apex of the Ag wedge, confirming the capability to precisely place individual emitters at desirable locations for quantum plasmonics (scale bar = 40 nm).

Figure 5e also includes a fit to the data (black line) using the dispersive plasmonic resonator model introduced in Figure 4. Strong agreement is obtained using the experimental L_{WPP} of 19 μm (Figure 3l) and $R = 93\%$. Because the electromagnetic simulations predict a propagation length of 29 μm and a reflectivity of 94% for our 600 nm high blocks, compared with previous experiments our results are clearly approaching the theoretical values. We note that good fits required us to add a Gaussian background in the model to account for photons that are emitted by the QDs and then scattered from the reflectors (see Section 7 in the Supporting Information). This non-plasmonic effect can also explain the lower finesse observed in the 7.5 μm cavity, where reflectors of the same height present a larger solid angle for scattering of emitted photons. Indeed, the experiments in Figure 5e–g used block heights of 600 nm because they offered high reflectivity for WPPs while minimizing this photon scattering.

The intensities and spectral positions of the measured cavity resonances (triangles in Figure 5e–g) are plotted in Figure 5h along with the QD-emission spectrum collected from the wedge but outside the cavity. The strong correlation confirms that the resonators are excited by the QDs. Figure 5i plots the same peak positions for each cavity relative to its shortest-wavelength feature. The resonances vary approximately linearly with wavelength, as expected for a Fabry-Pérot cavity. The slopes yield the expected FSRs for the different resonator lengths, in excellent agreement with our model. Further, every peak of the 7.5 μm cavity is resonant with every other mode of the 15 μm cavity.

When quantum emitters are efficiently coupled to such plasmonic resonators, their spontaneous-emission lifetime

should be strongly affected. We measured mean total lifetimes for our QDs using spatially resolved time-correlated single-photon counting (see Section 12 in the Supporting Information). We extracted lifetimes for seven different environments (Figure S11). In addition to a liquid dispersion (tetradecane), we printed QDs on glass, flat template-stripped Ag, Ag wedge waveguides, and Ag wedge resonators. The total lifetimes decreased from 16.7 ± 0.2 ns in tetradecane to 736 ± 38 ps on the resonator. In the latter case, we collected the signal from QD-generated WPPs that were scattered off the block reflector. Thus, this lifetime arises from QDs that are coupled to the cavity. The experiments yield a total lifetime reduction factor of 22.6 (if we compare “on resonator” to “in liquid”) or 12.4 (if we compare “on resonator” to “on glass”). For QDs at room temperature on a wedge resonator of the experimental length (6.5 μm), we predict a Purcell enhancement factor of 22.8. Our measured reduction factors (22.6 or 12.4) are therefore consistent with the predicted enhancement if we assume QD quantum yields of near unity on the wedge and $\sim 50\%$ on glass. Indeed, the quantum yield of our QDs, which is $\sim 90\%$ in liquid dispersion, is typically reduced to $\sim 50\%$ on glass because of exciton diffusion. On the wedge, where exciton migration can no longer compete with spontaneous emission, we would expect quantum yields to again approach unity. We note that the above discussion neglects the effect of any quenching to the metal, which we cannot measure. However, such quenching should be reduced in our QDs because of the spacing provided by their shells. (See Section 13 in the Supporting Information for more details on the Purcell effect and our analysis of the lifetime data.)

As discussed previously,^{51,52} in the limit when the emitter line width is broad compared with the cavity resonance (as in our case), the Purcell enhancement is constrained by the emitter line width. In the opposite limit (with extremely narrow emitters), one would expect higher Purcell enhancements (exceeding 100) for the same 6.5 μm cavity. Further, for a $\lambda/2$ cavity, values up to 1000 are expected (see Tables S1 and S2 in the *Supporting Information*). Single QDs at cryogenic temperatures, which can exhibit emission line widths 1000 times narrower than at room temperature,⁵³ would allow such enhancements to be explored.

In addition, if single QDs could be placed on the wedge waveguides, they would allow observation of coherent processes such as long-range entanglement of quantum emitters mediated by WPPs.^{13,47,48} Above we saw that the wedges can provide long propagation lengths and hence long coherence times. Also, small ensembles of QDs could be efficiently coupled to WPP modes such that their energy could be transmitted over extended distances. Quantum plasmonics requires the same capabilities but at the single-QD level.

By varying our printing conditions, we could place individual QDs on our wedge waveguides (see *Figure S12*). The fluorescence image in *Figure 6a* shows direct photon emission at room temperature (averaged over 1000 1 s frames; also see *Movie S1*) from three printed spots (labeled QD1, QD2, and QD3). The QDs at these locations also launch WPPs, which scatter weakly from the wedge end, seen at the top of the image. Time traces for photons detected from the wedge end (*Figure 6b*) and directly from QD2 (*Figure 6c*) reveal that the two signals are strongly correlated (>80%) and show on/off blinking behavior (highlighted in red and green, respectively) indicative of single-QD emission.⁵⁴ The on/off behavior is also revealed in the bimodal intensity histograms for the wedge end (*Figure 6d*) and QD2 (*Figure 6e*). These data indicate that QD2 is an individual quantum emitter that is well-coupled to the waveguide mode and launching WPPs. This is further illustrated in *Figure 6f* (*Figure 6g*) where 20 frames were averaged during a period that QD2 was off (on). The wedge end clearly becomes bright when QD2 turns on. Time traces for QD1 and QD3 (*Figure S13*) also show blinking behavior indicative of single QDs. However, their direct photon emission is less strongly correlated with the signal from the wedge end, suggesting that they are not as well coupled to the waveguide as QD2. Scanning electron micrographs collected after these experiments confirmed the presence of single QDs on the wedge apex (see *Figure 6h*).

Taken together, our results support earlier enthusiasm for plasmonic wedge waveguides. We have shown that such structures are well-suited to the exploration of single- and multiple-emitter quantum electrodynamics. We have demonstrated high-quality quantum emitters efficiently coupled to deep-subdiffraction single-mode waveguides that can then transmit quantum information over long distances. Without these capabilities, many coherent effects in quantum plasmonics and on-chip devices such as single-plasmon sources or quantum gates are unlikely to be realized. In comparison with other metallic resonators based on localized plasmonic modes, the wedge resonators also allow more flexibility in the tuning of their high-*Q* mode structure. Furthermore, in *Tables S1* and *S2*, we estimate the quality factor obtainable in practice, Q_{pract} , for a resonator with minimum volume, V_{\min} . The resulting dimensionless FOM $Q_{\text{pract}}/[V_{\min}/\lambda_{\text{vac}}^3]$, where λ_{vac} is the vacuum wavelength, exceeds 10^4 for all three metals considered

(Ag, Au, and Cu) at visible and near-visible wavelengths. We note that such values are ~30 times higher than those obtained in semiconductor microposts,^{4,55} optical cavities where many pioneering QED experiments with epitaxially grown QDs have been performed. We expect $V_{\min}/\lambda_{\text{vac}}^3$ to range from 0.004 to 0.007 at 630 to 1550 nm for our smallest Ag resonators. Such small modal volumes in an easily accessible single-mode plasmonic-waveguide system should enable novel experiments, particularly when combined with individual quantum emitters. A variety of coherent phenomena such as long-range quantum entanglement and strong coupling should emerge, leading to devices including quantum-plasmonic circuits, single-photon transistors, and quantum gates.

■ ASSOCIATED CONTENT

S Supporting Information

The Supporting Information is available free of charge on the ACS Publications website at DOI: [10.1021/acs.nanolett.5b03051](https://doi.org/10.1021/acs.nanolett.5b03051).

A detailed discussion of the experimental methods, electromagnetic simulations, and analyses ([PDF](#))

A movie showing photoluminescence blinking from the three individual quantum dots (QD1–3) shown in *Figure 6a* ([MOV](#))

■ AUTHOR INFORMATION

Corresponding Author

*E-mail: dnorris@ethz.ch.

Notes

The authors declare the following competing financial interest(s): D.P. is involved with a startup company that is attempting to commercialize the EHD NanoDrip printing process.

■ ACKNOWLEDGMENTS

We gratefully acknowledge funding from the European Research Council under the European Union's Seventh Framework Programme (FP/2007-2013)/ERC Grant Agreement 339905 (QuaDoPS Advanced Grant) and from the Swiss National Science Foundation under Grant 146180. We thank Jian Cui for experimental assistance, in particular with the single-QD studies.

■ REFERENCES

- (1) Loudon, R. *The Quantum Theory of Light*, 2nd ed.; Clarendon Press: Oxford, U.K., 1983; pp 226–249.
- (2) Anger, P.; Bharadwaj, P.; Novotny, L. *Phys. Rev. Lett.* **2006**, *96*, 113002.
- (3) Curto, A. G.; Volpe, G.; Taminiau, T. H.; Kreuzer, M. P.; Quidant, R.; van Hulst, N. F. *Science* **2010**, *329*, 930–933.
- (4) Vahala, K. J. *Nature* **2003**, *424*, 839–846.
- (5) Novotny, L.; Hecht, B. *Principles of Nano-Optics*, 2nd ed.; Cambridge University Press: Cambridge, U.K., 2012.
- (6) Maier, S. A. *Plasmonics: Fundamentals and Applications*; Springer Science: New York, 2007.
- (7) Novotny, L.; van Hulst, N. *Nat. Photonics* **2011**, *5*, 83–90.
- (8) Gramotnev, D. K.; Bozhevolnyi, S. I. *Nat. Photonics* **2013**, *8*, 13–22.
- (9) Barnes, W. L.; Dereux, A.; Ebbesen, T. W. *Nature* **2003**, *424*, 824–830.
- (10) Han, Z.; Bozhevolnyi, S. I. *Rep. Prog. Phys.* **2013**, *76*, 016402.
- (11) de Leon, N. P.; Lukin, M. D.; Park, H. *IEEE J. Sel. Top. Quantum Electron.* **2012**, *18*, 1781–1791.

- (12) Tame, M. S.; McEnery, K. R.; Özdemir, Ş. K.; Lee, J.; Maier, S. A.; Kim, M. S. *Nat. Phys.* **2013**, *9*, 329–340.
- (13) Hümmer, T.; García-Vidal, F.; Martín-Moreno, L.; Zueco, D. *Phys. Rev. B: Condens. Matter Mater. Phys.* **2013**, *87*, 115419.
- (14) Oulton, R. F.; Bartal, G.; Pile, D. F. P.; Zhang, X. *New J. Phys.* **2008**, *10*, 105018.
- (15) Min, B. K.; Ostby, E.; Sorger, V.; Ulin-Avila, E.; Yang, L.; Zhang, X.; Vahala, K. *Nature* **2009**, *457*, 455–459.
- (16) Schuller, J. A.; Barnard, E. S.; Cai, W. S.; Jun, Y. C.; White, J. S.; Brongersma, M. L. *Nat. Mater.* **2010**, *9*, 193–204.
- (17) Lamprecht, B.; Krenn, J. R.; Schider, G.; Ditlbacher, H.; Salerno, M.; Felidj, N.; Leitner, A.; Ausseneck, F. R.; Weeber, J. C. *Appl. Phys. Lett.* **2001**, *79*, 51–53.
- (18) Ditlbacher, H.; Hohenau, A.; Wagner, D.; Kreibig, U.; Rogers, M.; Hofer, F.; Ausseneck, F.; Krenn, J. *Phys. Rev. Lett.* **2005**, *95*, 257403.
- (19) Wild, B.; Cao, L.; Sun, Y.; Khanal, B. P.; Zubarev, E. R.; Gray, S. K.; Scherer, N. F.; Pelton, M. *ACS Nano* **2012**, *6*, 472–482.
- (20) Pile, D. F. P.; Gramotnev, D. K. *Opt. Lett.* **2004**, *29*, 1069–1071.
- (21) Bozhevolnyi, S. I.; Volkov, V. S.; Devaux, E.; Laluet, J. Y.; Ebbesen, T. W. *Nature* **2006**, *440*, 508–511.
- (22) Smith, C. L.; Thilsted, A. H.; Garcia-Ortiz, C. E.; Radko, I. P.; Marie, R.; Jeppesen, C.; Vannahme, C.; Bozhevolnyi, S. I.; Kristensen, A. *Nano Lett.* **2014**, *14*, 1659–1664.
- (23) Lee, J.; Song, J.; Sung, G. Y.; Shin, J. H. *Nano Lett.* **2014**, *14*, 5533–5538.
- (24) Bermúdez-Ureña, E.; González-Ballesteros, C.; Geiselmann, M.; Marty, R.; Radko, I. P.; Holmgård, T.; Alaverdyan, Y.; Moreno, E.; García-Vidal, F. J.; Bozhevolnyi, S. I.; Quidant, R. *Nat. Commun.* **2015**, *6*, 7883.
- (25) Pile, D. F. P.; Ogawa, T.; Gramotnev, D. K.; Okamoto, T.; Haraguchi, M.; Fukui, M.; Matsuo, S. *Appl. Phys. Lett.* **2005**, *87*, 061106.
- (26) Moreno, E.; Rodrigo, S.; Bozhevolnyi, S.; Martín-Moreno, L.; García-Vidal, F. *Phys. Rev. Lett.* **2008**, *100*, 023901.
- (27) Boltasseva, A.; Volkov, V. S.; Nielsen, R. B.; Moreno, E.; Rodrigo, S. G.; Bozhevolnyi, S. I. *Opt. Express* **2008**, *16*, 5252–5260.
- (28) Ogawa, T.; Pile, D. F. P.; Okamoto, T.; Haraguchi, M.; Fukui, M.; Gramotnev, D. K. *J. Appl. Phys.* **2008**, *104*, 033102.
- (29) Oulton, R. F.; Sorger, V. J.; Genov, D. A.; Pile, D. F. P.; Zhang, X. *Nat. Photonics* **2008**, *2*, 496–500.
- (30) Kolesov, R.; Grotz, B.; Balasubramanian, G.; Stohr, R. J.; Nicolet, A. A. L.; Hemmer, P. R.; Jelezko, F.; Wrachtrup, J. *Nat. Phys.* **2009**, *5*, 470–474.
- (31) de Leon, N. P.; Shields, B. J.; Yu, C. L.; Englund, D. E.; Akimov, A. V.; Lukin, M. D.; Park, H. *Phys. Rev. Lett.* **2012**, *108*, 226803.
- (32) Oulton, R.; Pile, D.; Liu, Y.; Zhang, X. *Phys. Rev. B: Condens. Matter Mater. Phys.* **2007**, *76*, 035408.
- (33) Sorger, V. J.; Oulton, R. F.; Yao, J.; Bartal, G.; Zhang, X. *Nano Lett.* **2009**, *9*, 3489–3493.
- (34) Akselrod, G. M.; Argyropoulos, C.; Hoang, T. B.; Ciraci, C.; Fang, C.; Huang, J.; Smith, D. R.; Mikkelsen, M. H. *Nat. Photonics* **2014**, *8*, 835–840.
- (35) Pompa, P. P.; Martiradonna, L.; Della Torre, A.; Della Sala, F.; Manna, L.; De Vittorio, M.; Calabi, F.; Cingolani, R.; Rinaldi, R. *Nat. Nanotechnol.* **2006**, *1*, 126–130.
- (36) Pacifici, D.; Lezec, H. J.; Atwater, H. A. *Nat. Photonics* **2007**, *1*, 402–406.
- (37) Chen, O.; Zhao, J.; Chauhan, V. P.; Cui, J.; Wong, C.; Harris, D. K.; Wei, H.; Han, H. S.; Fukumura, D.; Jain, R. K.; Bawendi, M. G. *Nat. Mater.* **2013**, *12*, 445–451.
- (38) Boldt, K.; Kirkwood, N.; Beane, G. A.; Mulvaney, P. *Chem. Mater.* **2013**, *25*, 4731–4738.
- (39) Khurgin, J. B. *Faraday Discuss.* **2015**, *178*, 109–122.
- (40) McPeak, K. M.; Jayanti, S. V.; Kress, S. J. P.; Meyer, S.; Iotti, S.; Rossinelli, A.; Norris, D. J. *ACS Photonics* **2015**, *2*, 326–333.
- (41) Hegner, M.; Wagner, P.; Semenza, G. *Surf. Sci.* **1993**, *291*, 39–46.
- (42) Nagpal, P.; Lindquist, N. C.; Oh, S.-H.; Norris, D. J. *Science* **2009**, *325*, 594–597.
- (43) Galliker, P.; Schneider, J.; Eghlidi, H.; Kress, S.; Sandoghdar, V.; Poulikakos, D. *Nat. Commun.* **2012**, *3*, 890.
- (44) Kress, S. J. P.; Richner, P.; Jayanti, S. V.; Galliker, P.; Kim, D. K.; Poulikakos, D.; Norris, D. J. *Nano Lett.* **2014**, *14*, 5827–5833.
- (45) Purcell, E. M. *Phys. Rev.* **1946**, *69*, 681.
- (46) Campbell, S. A. *The Science and Engineering of Microelectronic Fabrication*; Oxford University Press: New York, 2001.
- (47) Chang, D. E.; Sørensen, A. S.; Demler, E. A.; Lukin, M. D. *Nat. Phys.* **2007**, *3*, 807–812.
- (48) Martin-Cano, D.; Martin-Moreno, L.; Garcia-Vidal, F. J.; Moreno, E. *Nano Lett.* **2010**, *10*, 3129–3134.
- (49) Barnes, W. L. *J. Mod. Opt.* **1998**, *45*, 661–699.
- (50) Saleh, B. E. A.; Teich, M. C. *Fundamentals of Photonics*, 2nd ed.; Wiley: Hoboken, NJ, 2007.
- (51) Cocciali, R.; Boroditsky, M.; Kim, K. W.; Rahmat-Samii, Y.; Yablonovitch, E. *IEE Proc.: Optoelectron.* **1998**, *145*, 391–397.
- (52) Poitras, C. B.; Lipson, M.; Du, H.; Hahn, M. A.; Krauss, T. D. *Appl. Phys. Lett.* **2003**, *82*, 4032–4034.
- (53) Empedocles, S. A.; Norris, D. J.; Bawendi, M. G. *Phys. Rev. Lett.* **1996**, *77*, 3873–3876.
- (54) Nirmal, M.; Dabbousi, B. O.; Bawendi, M. G.; Macklin, J. J.; Trautman, J. K.; Harris, T. D.; Brus, L. E. *Nature* **1996**, *383*, 802–804.
- (55) Gerard, J. M.; Sermage, B.; Gayral, B.; Legrand, B.; Costard, E.; Thierry-Mieg, V. *Phys. Rev. Lett.* **1998**, *81*, 1110–1113.